Helicon volume production of H^- and D^- using a resonant birdcage antenna on RAID

Ivo Furno, Riccardo Agnello, Alan Howling, Philippe Guittienne, Remy Jacquier, Christine Stollberg, Marcelo Baquero, Lyes Kadi, Claudio Marini, Jia Han, et al.

Chapter 9
Helicon Volume Production of H^- and D^- Using a Resonant Birdcage Antenna on RAID

Ivo Furno, Riccardo Agnello, Alan Howling, Philippe Guittienne, Remy Jacquier, Christine Stollberg, Marcelo Baquero, Lyes Kadi, Claudio Marini, Jia Han, Stéphane Béchu, Gwenael Fubiani, Alain Simonin, and Francesco Taccogna

Abstract Negative ion production by volumetric processes is investigated in the RAID linear device using experiments and modeling. Measurements by optical emission spectroscopy, cavity ring-down spectroscopy, and Langmuir probe assisted laser photodetachment are combined and reveal that H^- and D^- ions are distributed in a halo around the plasma column with densities of 2×10^{16} m^{-3} for only a few kilowatts of RF power in a Cs-free plasma. A hydrogen transport fluid code shows that RAID plasmas have a hot electron core favorable to ro-vibrational excitation and dissociation of H_2 molecules. Dissociative attachment to ro-vibrationally excited H_2 molecules is the only significant source of H^- anywhere in the RAID volume.

Keywords Helicon plasmas · RAID · Resonant antennas · Negative ion diagnostics · Volume production · Fluid simulations

I. Furno · R. Agnello · A. Howling · P. Guittienne · R. Jacquier · C. Stollberg · M. Baquero · L. Kadi · C. Marini · J. Han
Swiss Plasma Center (SPC), Ecole Polytechnique Fédérale Lausanne (EPFL), Lausanne, Switzerland
e-mail: ivo.furno@epfl.ch

S. Béchu
Université Grenoble-Alpes, CNRS, Grenoble INP, LPSC-INP23, Grenoble, France

G. Fubiani
LAPLACE, CNRS, Université de Toulouse, Toulouse, France

A. Simonin
CEA, IRFM, St-Paul-lez-Durance, France

F. Taccogna (✉)
Institute for Plasma Science and Technology, CNR, Bari, Italy
e-mail: francesco.taccogna@cnr.it

M. Bacal (ed.), *Physics and Applications of Hydrogen Negative Ion Sources*,
Springer Series on Atomic, Optical, and Plasma Physics 124,
https://doi.org/10.1007/978-3-031-21476-9_9

9.1 Introduction

Since the first experiments performed by Boswell (1970), helicon sources have been extensively studied and they are proven to be very efficient for high-density plasma production, electron density $= 10^{18} - 10^{19}$ m^{-3} (in noble gases, typically argon) with moderate injection power at low pressure. Historically, they have found applications in semiconductor manufacturing and ion thruster systems.

From its beginnings in 2017, the Resonant Antenna Ion Device (RAID) at the Swiss Plasma Center of EPFL (École Polytéchnique Fédérale de Lausanne), Switzerland, has been operated to explore the main technology and physics issues related to high-power, steady-state helicons. In this chapter, we describe the experimental activities on RAID to investigate the formation of negative ions by volumetric processes in H/D helicon plasmas. With a continuously improving set of state-of-the-art diagnostics and of theoretical and modeling tools, research on RAID has today reached a level at which quantitative comparisons between theory and experiment can be performed. This has resulted in a better understanding of the complex plasma chemistry involved in H/D discharges as well as of helicon wave generation by resonant antennas.

This chapter is organized as follows. In Sect. 9.2, a description of RAID and its main ancillaries is provided. Section 9.3 details the principal diagnostics used to study negative ion physics. Section 9.4 summarizes the most salient measurements of negative ions using a combination of these diagnostics. The development and first results of a hydrogen transport fluid model are presented in Sect. 9.5 to interpret the experimental results. Finally, summary and outlook are given in Sect. 9.6.

9.2 The Resonant Antenna Ion Device (RAID)

RAID generates a cylindrical plasma column along a linear magnetic field, producing steady-state helicon plasma discharges in various gases including H_2 and D_2 (Furno et al. 2017; Agnello et al. 2018, 2020; Marini et al. 2017) as well as He, Ar, N_2, and Ne for a wide range of plasma physics investigations (Thompson et al. 2017). A photograph of RAID is shown in Fig. 9.1a. The red glow from the cylinder on the left is the plasma emission seen through the water-cooled ceramic tube (it is not red hot) surrounded by the resonant antenna generating the plasma. Figure 9.1b shows the visible light emission from a typical hydrogen plasma discharge. This picture is taken from the end of the plasma column near the target through an off-axis viewport. The plasma column impinges on a target, also partially visible in the picture. In this section, the RAID experimental apparatus is described together with its main ancillaries and diagnostics.

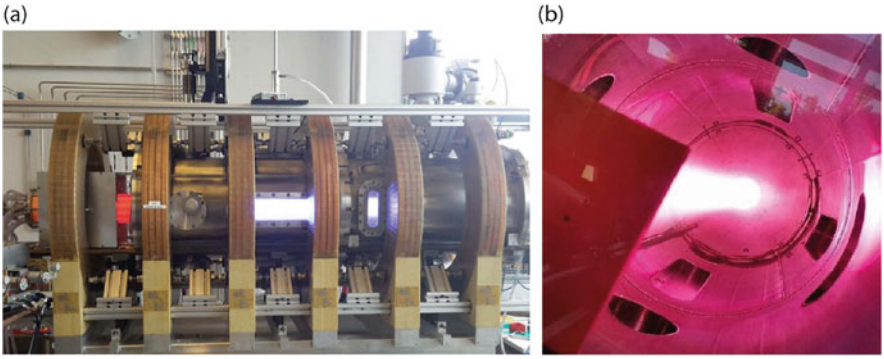

Fig. 9.1 Pictures of the RAID experiment at the Swiss Plasma Center of École Polytechnique Fédérale de Lausanne. (**a**) The RAID vacuum vessel is surrounded by six water cooled coils. (**b**) Downstream view of a visible light emission from a typical plasma column in hydrogen. The target is partially visible in the foreground

9.2.1 RAID Vacuum Vessel, Pumping System, and Magnetic Field

Figure 9.2 shows a schematic drawing of RAID with its main elements. The stainless vacuum vessel is linear (1.9 m total length and 0.4 m internal diameter) and is made of two movable sectors with multiple diagnostic access and it is surrounded by six water-cooled magnetic field coils. The vacuum vessel is also water-cooled and allows for long-time (up to days) continuous operation with stable and reproducible plasma conditions. The pumping system consists of a primary rotary pump and a turbopump located on the top-right of the vessel. The gas pressure is regulated by mass flow controllers at a constant turbo pumping speed of 170 l/s corresponding to a baseline gas pressure of better than 7×10^{-6} mbar. The six magnetic field coils generate an axial magnetic field (up to 800 G on axis), which is needed to propagate helicon waves (Guittienne et al. 2021) and to radially confine the plasma. RAID operates with two separate groups of identical coils, a source coil, the first coil on the left in Fig. 9.2, and five vessel coils. The distance between each coil is $21(\pm 0.5)$ cm to optimize the axial homogeneity of the magnetic field. Two DC power supplies feed the two sets of coils with a current ripple lower than 1%. The coils are actively cooled by forced water convection in the copper pipes allowing for continuous operation. Each coil is made of 9(radial) $\times$ 4(axial) turns with a central channel for water cooling. The coil internal and external diameters are 52 cm and 82.6 cm, respectively. Each turn is electrically isolated with resin. The coil ohmic resistance is $\sim$5 mΩ and its inductance is $\sim$6.4 mH. More details on the coils can be found in Müller et al. (2007). The polarity of the source coil can be reversed with respect to the other five coils, to create a divergent magnetic field at the antenna position. This promotes plasma ignition and stabilizes the helicon regime, resulting in a stable plasma over a wider operational space. The reason for this improvement is not well

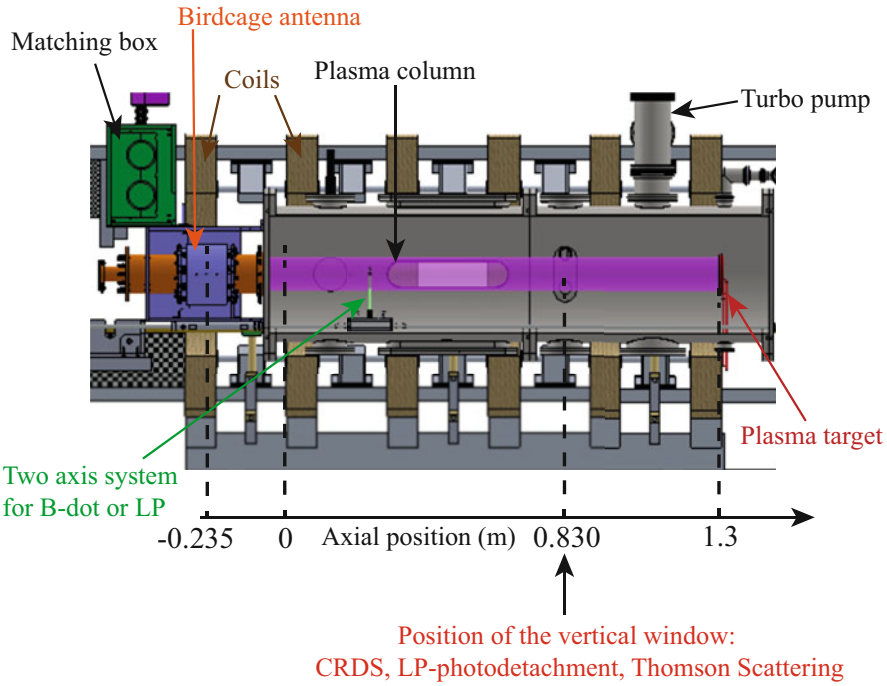

Fig. 9.2 Schematic of the Resonant Antenna Device including the location of the main diagnostics

understood but might be due to the effect of a magnetic field gradient helping to confine slower electrons in the antenna region thus enhancing the ionization.

Figure 9.3 shows the spatial and on-axis magnetic field produced in standard conditions (see below for the definition of standard conditions), namely with −40 A in the source coil (producing a counter-field) and 150 A in the vessel coils. The on-axis magnetic field intensity shows a strong gradient in the antenna region, a peak at 20 mT in the center of the vessel, and a decay to 10 mT at the target position. Most helicon sources operate with uniform magnetic fields, even though the propagation of helicon waves in divergent magnetic field geometries was also investigated (Takahashi et al. 2016). When only the source coil is turned on, the plasma is partially transported in the main chamber; when all coils are turned off, the plasma coupling is purely inductive and the plasma is confined in the region of the ceramic tube corresponding to the antenna length.

9.2.2 RAID Plasma Source: The Birdcage Antenna

RAID plasmas are ignited and sustained by an innovative helicon source consisting of a resonant network antenna. This antenna has a birdcage geometry (Guittienne

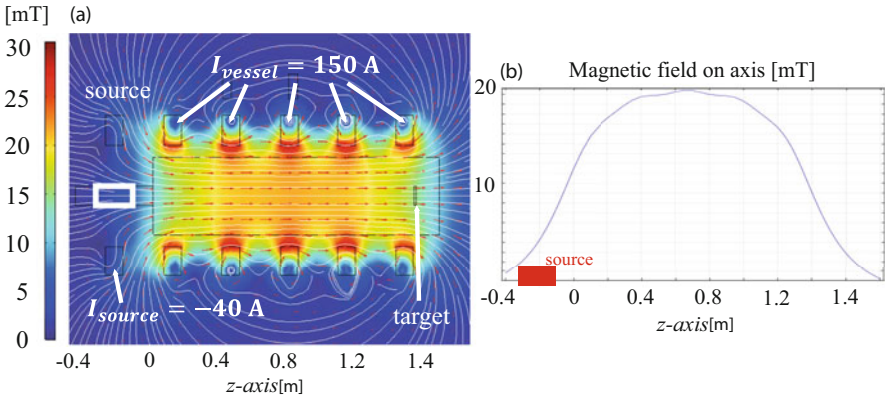

Fig. 9.3 (**a**) Magnetic field mapping in standard conditions: −40 A in the source coil (counter field) and 150 A in the vessel coils and (**b**) intensity of the magnetic field on axis for same parameters and axial position of the antenna in red. At the maximum axial field strength near $z = 0.7$ m, the magnetic field is almost uniform over the vessel cross-section, falling by 1% at $r = 0.1$ m and by 10% at the wall, $r = 0.2$ m

et al. 2005, 2021), shown in Fig. 9.4, and is installed on the left end-flange of the device (Fig. 9.2). Its length is 15 cm, its center is at the axial position $z = -0.235$ m, and it surrounds the ceramic tube. The ceramic tube is made of an assembly of two coaxial tubes (internal diameter 9.5 cm and external diameter 11.5 cm) made of alumina, Al_2O_3. Between the two tubes, there are 8 equally spaced channels for water cooling, necessary to avoid vacuum joint melting. After many hours of continuous operation, the internal surface of the ceramic shows no sign of sputter damage, with no more than a thin dark coating which could be of metallic origin. Faraday screens are therefore not necessary because the low-amplitude RF plasma potential induced by the birdcage does not form a high voltage sheath with high-energy ion bombardment. Alternatively, the ceramic tube can be mounted with a half-helix antenna whose dimensions are very similar to the birdcage antenna. The birdcage antenna is commonly used in nuclear magnetic resonance for excitation and detection. In helicon wave physics, different antenna configurations were developed with the main idea to match the RF field generated to the helicon wave field in plasma, such as Nagoya, half-helix, Boswell type, and paddle shaped (Chabert and Braithwaite 2011). Since the helicon field has a rotating pattern, these antennas are usually in a twisted geometry to enhance the matching. The birdcage antenna is designed to generate a rotating azimuthal distribution of RF currents. It features 9 parallel copper bars, of inductance L and resistance R, in cylindrical geometry. The end of each leg is connected to its closest neighbors via mica capacitors of C = 3840 pF. The birdcage antenna has a resonant frequency which is specific to the geometric arrangement and the impedance of its components. When it is excited by a radiofrequency source, an azimuthal sinusoidal distribution of oscillating currents is generated in the antenna legs. The R, L, C values are chosen

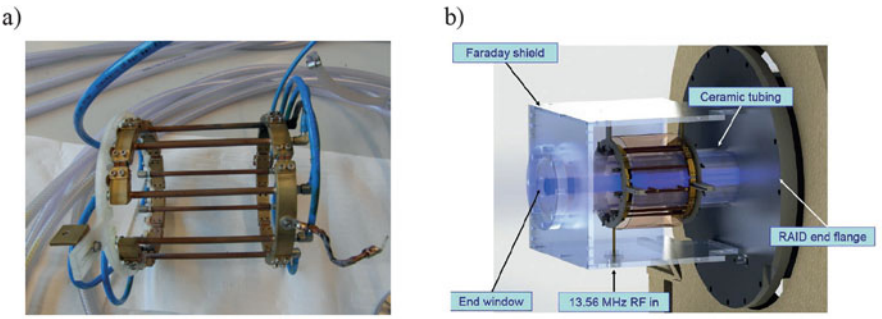

Fig. 9.4 (**a**) Picture of the birdcage antenna showing the copper legs, the position of the capacitors, and the tubes for water cooling. (**b**) Location of the birdcage antenna mounted on the ceramic tubing at the RAID and flange. The antenna is enclosed in a Faraday screen to limit RF emissions

Table 9.1 RAID general machine and plasma parameters

Device parameters		Plasma parameters	
Antenna type	Birdcage/Half-helix	Electron density n_e	10^{16}–10^{19} m^{-3}
Antenna length	15 cm	Plasma width (FWHM of n_e)	6 cm
RF power (nominal)	0.3–10 kW cw	Electron Temperature	1–10 eV
Magnetic field on axis	50–800 G	Ion Temperature	~0.1 eV
Gas species	H_2, D_2, Ar, He, N_2, Ne	Ion Flux (on target)	$\sim 10^{21}$ m^{-2}s^{-1}
Pressure	0.15–1 Pa	Power Flux (on target)	~100 kW/m^2

so that it resonates close to 13.56 MHz, a standard industrial frequency. Extensive treatment of birdcage theory can be found in Refs. Guittienne et al. (2005, 2021).

9.2.3 *Plasma Parameters in RAID and Standard Conditions*

Table 9.1 summarizes the ranges of device and plasma parameters. Plasma columns have peaked radial profiles in n_e and T_e, with typical FWHM of 6 cm along the radial direction. The source is usually operated with the parameters listed in Table 9.2; we define "standard conditions" as follows: 0.3 Pa pressure measured during the plasma by a capacitive gauge mounted on the vacuum vessel; a current in the vessel coils of 150 A and −40 A in the coil surrounding the antenna, also called counter-field coil. Plasmas in standard conditions have fewer density fluctuations, and the RF power for ignition is minimized. In standard conditions and 3 kW RF power, the peak electron density is about $\sim 2 \times 10^{18}$ m^{-3} for H_2 or D_2 and $\sim 1 \times 10^{19}$ m^{-3} for argon. Furthermore, a stable helicon plasma is obtained with only 300 W in argon and 1000 W in hydrogen and deuterium. The operation with light molecule plasmas is more difficult compared to heavy atom plasmas because: (1) the Bohm velocity, $u_B = \sqrt{k_b T_e / m_i}$, is larger for light ion plasmas, leading to larger axial losses and

Table 9.2 RAID "standard conditions" for H_2 or D_2 plasma discharge

Gas pressure	0.3 Pa	RF power	1–8 kW
Vessel peak field	200 G	Vessel coils current	150 A
Field in antenna center	30 G	First coil current	−40 A
Birdcage boundary	Dielectric	Downstream boundary	Floating

(2) when molecular gases are used, a large fraction of the antenna power is used to excite the ro-vibrational channels or to dissociate the molecule (Hjartarson et al. 2010). In RAID, H_2 plasma ignition cannot be achieved with H_2 alone. Instead, the plasma is first ignited using a mixture of H_2 and Ar, and then the Ar gas flow is stopped resulting in a pure H_2 plasma.

9.3 Overview of RAID Diagnostics

RAID is equipped with basic plasma diagnostics as well as sophisticated state-of-the-art systems, enabling a full characterization of the various plasma components (electrons, ions, molecules, etc.).

9.3.1 Diagnostics of Electron Parameters

The relatively low temperatures and densities of RAID plasmas, in some regimes, allow the use of Langmuir probes (LPs) to measure the electron density and temperature profiles across the entire device. However, LPs suffer strong heating for an electron density larger than a few $10^{18}\,m^{-3}$, which is achieved in argon for a relatively low RF power (∼600 W) and in hydrogen or deuterium for about 3000 W RF power. This limits the use of LPs to the edge of the plasma column and to low RF powers. To overcome this limitation, microwave interferometry and incoherent Thomson scattering are used in parallel with LPs, allowing to probe all RAID plasma regimes as well as to extract absolutely calibrated electron density profiles. These techniques and the experimental setup on RAID are described in this section.

Langmuir Probes (LP) Electron density and temperature along the vessel are measured by means of LPs mounted on a two-axis system (Fig. 9.2), which can scan axially and radially inside the plasma column holding either a LP or a B-dot magnetic coil probe (Jacquier et al. 2019). Single tip LPs, RF compensated LPs, as well as double tip LPs are used depending on the plasma conditions.

Microwave Interferometry Measurements of electron density can also be performed using a heterodyne microwave interferometer. 100 GHz mm-waves are

injected into the plasma, and the phase change is directly related to the line-integrated value of n_e along the mm-wave beam. By vertically displacing the system, one can then obtain absolute line-integrated measurements of n_e at different positions. In combination with LP data, these measurements are used to obtain absolute electron density radial profiles, which can be compared with TS data.

Thomson Scattering (TS) This non-intrusive technique is used to measure the electron velocity distribution function (EVDF), thereby providing the electron temperature and possible drift velocity, as well as the absolute calibrated electron density. The setup operates in the incoherent scattering regime, where the photon energy is altered solely due to the Doppler shift by the free electron velocity in the plasma along the probe vector. A preliminary system used polychromators and a 1064 nm laser (Agnello et al. 2020). The improved TS system uses a spectrometer and a 532 nm laser focused to 1 mm beam diameter. The scattered radiation is collected with a spatial resolution of 4 mm along the laser beam at a 90° scattering angle and is guided to a high-throughput spectrometer (FL = 200 mm, 2400 l/mm) by an optical fiber. A photo multiplier tube (PMT) with a rise time of 0.57 ns detects the scattered light. The spectrum is scanned by varying the spectrometer grating angle. The setup has a spectral resolution of 0.8 nm and can therefore measure electron temperatures >0.4 eV. A satisfactory signal-to-noise ratio is achieved by collecting up to 20,000 laser shots per wavelength. The uncertainties of the measured electron parameters are obtained from a Bayesian analysis approach, which also evaluates cross correlations between different parameters.

9.3.2 Diagnostics for Negative Ions: Optical Emission Spectroscopy, Cavity Ring-Down, and Photodetachment

Negative ions in plasmas could be theoretically detected by LPs by measuring the shape of the second derivative of the current–voltage probe characteristic. This technique is used when the plasma electronegativity $\alpha = n_-/n_e$ is about 1 or more (Popov et al. 2013). However, in the case of low-temperature hydrogenic plasmas, the electronegativity is of the order of 0.1, and the negative ion density is too small, resulting in too noisy I–V curves. Therefore, the measurements of negative ions in such plasmas require other dedicated techniques.

The measurements of negative ions in RAID are performed by direct techniques such as Cavity-Ring Down Spectroscopy (CRDS) and LP Laser Photodetachment (LPLP). These techniques are routinely employed in negative ion sources for fusion (Berger et al. 2009; Christ-Koch et al. 2009; Fantz et al. 2006) but have rarely been employed in helicon plasma devices. Indirect techniques, such as optical emission spectroscopy (OES) supported by collisional radiative codes, are also used on RAID. These techniques as well as the experimental setup on RAID including the technical challenges are reviewed below.

9.3.2.1 Optical Emission Spectroscopy (OES)

Passive spectroscopic measurements of Balmer and Lyman lines and of the Fulcher-α bands are performed with an f/2 spectrometer, for both hydrogen and deuterium (Marini et al. 2017). The setup consists of a field lens coupled via an optical fiber bundle to a high-throughput spectrometer and a detector. The input optics is a Navitar f/1.4 35 mm lens, and the image focal plane is optimized to image the RAID axis at 25 cm from the lens. The input lens is mounted on a RAID lateral port to sample the plasma column at different axial positions along the device. The fiber bundle is composed of 19 fibers of numerical aperture 0.22, with a fused silica core of diameter 365 μm. The diameter of their adjacent images on the focal plane is 2.9 mm, resulting in a 55.1 mm wide sampling region. Collected light is analyzed by a high-throughput spectrometer, which is composed of two Nikon f/2 200 mm lenses and a Horiba holographic grating of 2400 lines per mm groove density blazed at 400 nm. This is sufficient to resolve most of the Fulcher-α molecular lines. The spectrometer uses an Andor iXon Ultra 897 camera, which features a back-illuminated 512×512 pixel frame transfer sensor and an optional electron multiplying (EM) readout register. The multiple viewing lines and an absolute intensity calibration are tomographically inverted to determine the absolute plasma radiance profile with a spatial resolution <3 mm.

9.3.2.2 Cavity Ring-Down Spectroscopy (CRDS)

In CRDS, first introduced by O'Keefe to measure absorption spectra (O'Keefe and Deacon 1988), a light pulse bounces multiple times between two high reflectivity (HR) mirrors to measure the medium absorbance. The main features of CRDS are that it is very sensitive, directly measures the number density of the species of interest, and is independent of the intensity of the light source. The main element of a CRDS system is the optical cavity made of two HR mirrors between which the light undergoes multiple reflections, thus multiplying the interaction length of the light with the absorbing medium. CRDS can be applied as a plasma diagnostic to measure the number density of different plasma species. In fusion, it is particularly interesting for the detection of H^- and D^- in negative ion sources (Berger et al. 2009; Nakano et al. 2016).

In RAID, to measure H^- and D^- densities, the employed light source is a pulsed Nd:YAG laser whose photon energy ($E = 1.2$ eV, corresponding to a wavelength of $\lambda = 1064$ nm) is large enough to strip the weakly bound electron of H^- ($E_{binding} = 0.75$ eV) by photodetachment, $h\nu + H^- \rightarrow H + e$. The light reflected back and forth inside the cavity is lost both because of the transmission of the mirrors and the presence of an absorbing medium along the line of sight (LOS) of the laser. The signal leaking through the cavity consists of a train of pulses whose intensity shows an exponential decay $I(t) = I_0 e^{-t/\tau}$, where I_0 is the initial intensity and τ can be expressed as $\tau = \frac{L}{c(1-R+\alpha d)}$, where L is the cavity length, c the speed of light, and R the reflectivity of the mirrors. The absorption coefficient is given by $\alpha = \bar{n}_{H^-}\sigma_{H^-}$,

where σ_{H^-} is the interaction cross-section ($\sigma_{H^-} = 3.5 \times 10^{-21}$ m^2 at a wavelength of 1064 nm) and $\bar{n}_{H^-}$ is the H^- line-integrated density. d is the path length of the laser beam in the absorbing medium and is usually the parameter known with the least accuracy. The line-averaged density $\bar{n}_{H^-}$ is

$$\bar{n}_{H^-} = \frac{1}{\sigma_{H^-}} \frac{L}{cd} \left(\frac{1}{\tau} - \frac{1}{\tau_0} \right), \tag{9.1}$$

where τ_0 and τ are the values of the decay time in the absence and presence of absorbing medium (H^-/D^-), respectively.

9.3.2.3 CRDS Experimental Setup in RAID

OES measurements first suggested that negative ions are distributed on a radial shell ~1 cm thickness with the radial center of the layer at ≈ 4 cm for a H_2 plasma. At this radial location, we expect a higher density of negative ions than on-axis because the electron temperature drops to 1–2 eV, which reduces dissociative attachment. We then decided to explore this radial shell by CRDS.

Figure 9.5 shows a picture of the experimental setup of the CRDS in RAID, from the laser injection side (Agnello et al. 2018). In Fig. 9.5a, the laser beam (in red) passes through the optical insulator, it is reflected by three mirrors, and it is finally injected into the cavity. Approximately 4% of the impinging laser energy enters the cavity. From the detection side, in Fig. 9.5b, the detector measures the light leaking from the cavity. The detector objective is connected to the mirror mounting with a conical adapter. Figure 9.6a and b shows a schematic of the CRDS experimental setup installed on RAID. The optical cavity is 91 cm long, enough to avoid overlapping of the laser pulses inside the cavity, which may result in multiple cavity modes and then in a non-exponential decay of the measured ring down signal.

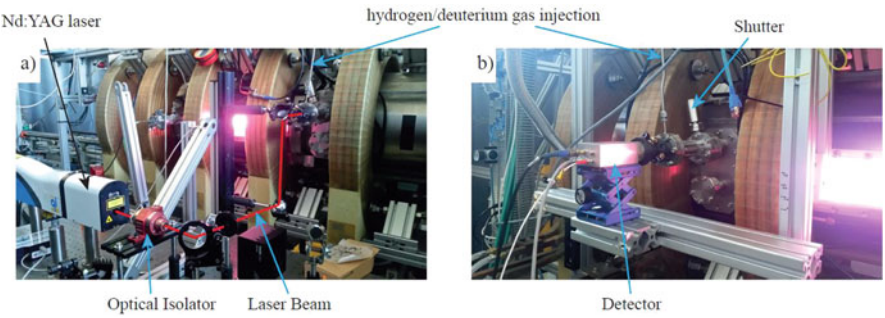

Fig. 9.5 Photo of the CRDS experimental setup in RAID: (**a**) injection side of the laser: the laser beam passes through the optical isolator, is reflected by three mirrors, and is injected inside the optical cavity. (**b**) Detection side: the detector collects the light leaking the optical cavity

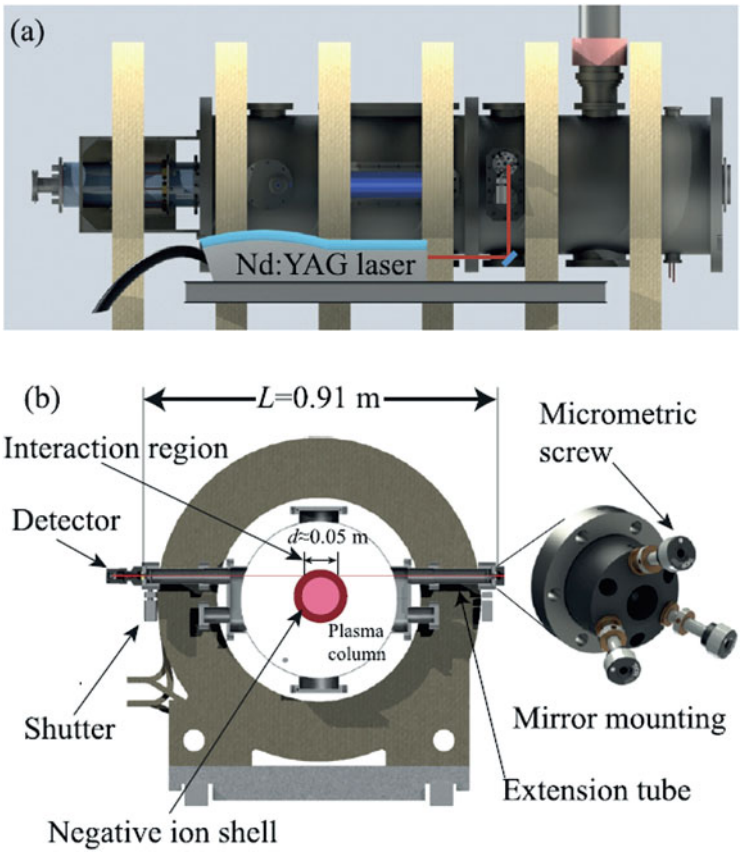

Fig. 9.6 (**a**) Side view of RAID: the laser beam is steered and enters the optical cavity perpendicular to the RAID axis. (**b**) Transverse section of RAID in the CRDS plane: the line of sight of the laser beam (schematically shown in red) is 4 cm displaced from the plasma column center so that it traverses the negative ion shell (as expected from OES measurements (Marini et al. 2017)). Reproduced from *Review of Scientific Instruments* **89**, 103504 (2018); doi: 10.1063/1.5044504, with the permission of AIP Publishing (Agnello et al. 2018)

The HR mirrors are positioned on vacuum tight mirror mountings on two tube extensions. This is also to minimize the solid angle of exposure of the mirrors to the plasma. To limit the exposure time of the mirrors to the plasma, a mechanical shutter in each extension is closed when the CRDS is not operational. Moreover, to reduce the effect of energetic particles impacting the mirror HR coating, the feeding hydrogen gas is flushed in front of the HR mirrors. Argon, which is needed to facilitate the plasma ignition, is injected from the back flange of the helicon antenna.

First measurements were performed with D_2 plasmas in standard conditions to compare with past OES measurements (Marini et al. 2017). The technique consists in measuring τ before, during, and after a plasma discharge. A typical

τ measurement in a D_2 plasma at 5 kW RF power and with an argon plasma at 700 W RF power is shown in Fig. 9.7a, b, respectively. The entire time range for the deuterium is divided into four intervals marked by the letters A, B, C, and D.

In Fig. 9.7a, during the first 300 s (interval A), only D_2 gas is present and the RF power is off. Argon gas is injected to facilitate plasma ignition a few seconds before it. At $t = 300$ s, the plasma discharge is initiated and the argon gas flow is progressively decreased. During this period of 50 s, τ_D decreases due to the combination of D^- absorption and a thermal effect on the cavity. After $t = 350$ s, only D_2 is injected and maintained stable for about 150 s (interval C). Then, the plasma is turned off at $t = 500$ s when τ_D exhibits a jump from 34.8 µs to 37.1 µs between two consecutive acquisitions (see zoom box at $t = 500$ s in Fig. 9.7a) due to the sudden disappearance of D^-. Finally, τ_D tends to its value before the plasma discharge (interval D).

As one can clearly see in Fig. 9.7a, together with the rapid jump due to the plasma extinction, a slower variation can be observed, lasting some minutes after the plasma is turned off. τ_D takes more than 10 min to recover to its initial value before the plasma discharge. Even during the plasma D_2 discharge, τ_D is observed to drift. These long period drifts are most likely due to thermal effects causing a distortion of the optical cavity.

To verify that the sudden jump observed at $t = 500$ s in Fig. 9.7a is due to the disappearance of negative ions, a test with an argon plasma of similar electron density, not contributing to laser absorption, was performed. No jump occurred when the argon plasma was turned off (see zoom box in Fig. 9.7b), confirming that the jump seen in D_2 plasma is due to the disappearance of negative ions produced in this plasma. A gradual drop $\delta\tau_{Ar}$ of about 0.5 µs, at the limit of the sensitivity, is observed when the argon plasma is turned on. This is probably due to a loss of alignment caused by the thermal expansion of the cavity. When the argon plasma is turned off, τ_{Ar} recovers slowly to its pre-discharge value after some minutes. Thus, the fast dynamics of τ that characterizes the plasma extinction (of the order of 100 µs), with respect to the slow drift of optical cavity thermal expansion, can be taken as a signature of the negative ion disappearance in H_2 and D_2 plasmas. By making a linear fit of τ_D a few seconds before and after the τ_D jump (see Fig.9.7a), the D^- density can be calculated. In this way, any fast transient effects (10^1 µs) on negative ion density (Hopkins and Mellon 1991) at plasma extinction are avoided. The error on the calculation of $\bar{n}_{D^-}$ is estimated using the errors on the coefficients of the linear fit. An average density $\bar{n}_{D^-}$ of $(3.05 \pm 0.09) \times 10^{16}$ m^{-3}, on a 5 cm path length, is deduced; this value is comparable to the results of OES in hydrogen. To summarize, the CRDS diagnostic measured D^- density in agreement with previous OES measurements. Further results are shown in Sect. 9.4.2.

9.3.2.4 Langmuir Probe Laser Photodetachment (LPLP)

CRDS at a fixed measurement position is not sufficient to determine the local negative ion density since its signal results from the interaction of the laser beam

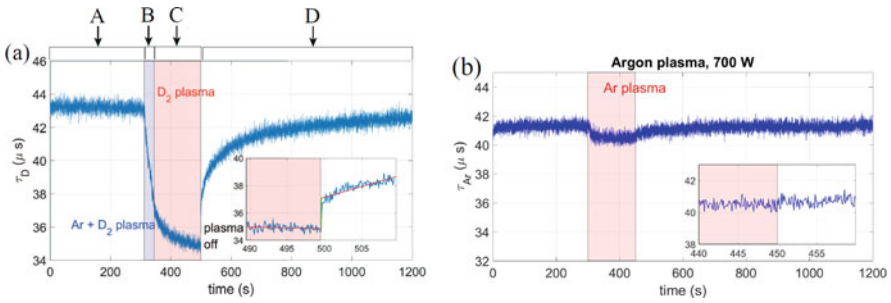

Fig. 9.7 The time evolution of τ before, during, and after the plasma discharge for (**a**) D_2 5 kW plasma and (**b**) Ar 700 W plasma, at 0.3 Pa. Red areas show when the plasma is on. The box inset is a zoom around the instant when the plasma is turned off ($t = 500$ s for D_2 and $t = 450$ s for Ar). The D_2 exhibits a jump due to D^- disappearance (zoom box in (**a**)), while no jump is observed for the Ar plasma (zoom box in (**b**)). Reproduced from *Review of Scientific Instruments* **89**, 103504 (2018); doi: 10.1063/1.5044504, with the permission of AIP Publishing (Agnello et al. 2018)

along the whole path intersecting the plasma. Moving the laser beam across the plasma column could be used to Abel invert the data to reconstruct the n_- radial profile by assuming cylindrical symmetry. However, this method is impractical due to the lengthy alignment procedure. LPLP can alternatively be used to obtain relative negative ion profiles with a spatial precision comparable to the laser beam diameter. A full review of LPLP can be found in Bacal (2001); Baghiti-Sube et al. (1996); here, we briefly review the basic purposes of LPLP and its implementation on RAID (Agnello et al. 2020).

In H^- or D^- ions, the extra electron is weakly bound to the atom. A laser pulse with sufficient energy can photodetach a large number of electrons from the negative ions along the laser path in the plasma. A laser requires a relatively low energy flux ($\sim$10 mJ/cm^2) to photoneutralize all H^- or D^- ions along its path (Bacal 2001). Moreover, since the laser pulses are very short ($\sim$5 ns in RAID), the photodetachment process happens on a time scale much shorter than that of the plasma evolution, allowing to temporally resolve the negative ion density. LPs can be employed to measure both the photodetached electrons and the local plasma density (Bacal 2001). The LP probe is coaxial with the axis of the laser beam and biased at a potential V_{LP} higher than the local plasma potential V_p. When $V_{LP} > V_p$, the LP draws a current I_{dc}, proportional to the local electron density n_e. The laser pulse causes a very fast increase of the detected current over a few ns, I_{pd}, proportional to the number of photodetached electrons. The negative ion density n_- can then be estimated by $n_-/n_e = I_{pd}/I_{dc}$.

Figure 9.8a shows a picture of the experimental setup of the LPLP system on RAID. Unlike the CRDS setup, the laser beam measurement position is not constrained by the position of the HR mirrors but can be vertically displaced along the window. The laser pulses are produced by the same Nd:YAG laser described in Sect. 9.3.2.3 and injected into the vacuum vessel by an optical beam path similar to that used for CRDS but with varying injection position. To detect the photodetached

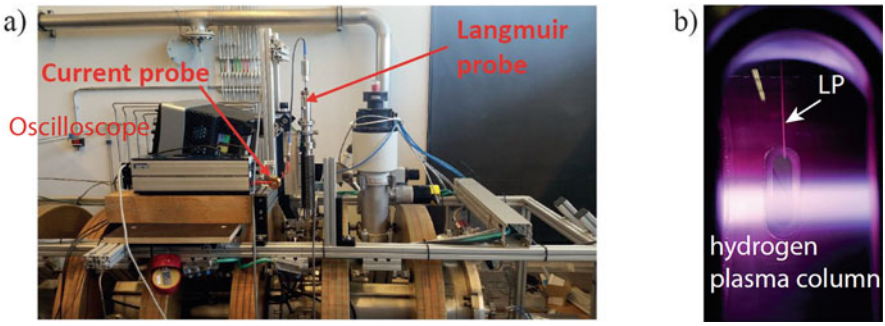

Fig. 9.8 (**a**) Experimental setup for LPLP measurements in RAID showing the positioning of the LP, of the current probe and of the oscilloscope. (**b**) Picture of the interior of the vessel showing a hydrogen plasma column and the location of the Langmuir Probe for photodetachment measurements

electrons, a LP moving in the vertical direction is employed. The probe is displaced by a stepper motor, and the vacuum is maintained by a bellows. The probe tip is L-shaped co-axially aligned with the direction of the laser beam. The probe is biased at $V_{\text{bias}} = 26\,\text{V}$ above the plasma potential, which is $V_{\text{plasma}} = 12\,(\pm 1)\,\text{V}$ for $r < 0.06\,\text{m}$, for both H_2 and D_2 plasmas, and independent of gas pressure. Figure 9.8b shows a picture of the ceramic stick of the LP probe inside the vessel, at its most external radial position ($r_{max} = 10\,\text{cm}$).

To measure at different radial locations in the plasma column, the LP and the laser measurement position have to be simultaneously displaced. The laser beam and LP tip are aligned at each measurement position by vertically displacing the reflecting laser beam injection mirror and the LP by the same distance. Alignment is obtained by detecting the laser beam spot after the exit window by flash paper and the shadow of the LP tip on the beam spot can be seen. The length of the vertical windows allows measurement of the cross-section plasma column up to $r_{max} = 7\,\text{cm}$. To filter out the DC component of the signal collected when the probe bias is at V_{bias} from the fast transient due to the photodetachment, we employ an AC toroidal current transformer with 2.5 V/A sensitivity and upper cut-off frequency at 1.17 GHz. Signals are acquired by an oscilloscope mounted on the top of RAID (see Fig. 9.8a) to minimize the length of the cable to avoid parasitic capacitance effects. Photodetachment signals are usually acquired in a few microseconds temporal window with a sampling rate of 10 GS/s. Signals are triggered by a photodiode sensitive to the laser wavelength detecting the passage of the laser pulse before entering the vessel. The noise level on the single LPLP signal is such that averaging over several hundred acquisitions is usually required.

Typical photodetachment signals are shown in Fig. 9.9 for different powers. The laser pulse strikes the LP tip at $t = 0\,\text{s}$ causing the overshoot (increase of the collected electron current) whose amplitude is indicated by the vertical arrow for the 5 kW case. The subsequent undershoot and the lack of "plateau" have been reported by other authors such as by P. Devynck et al. (1989), M. Bacal (2001),

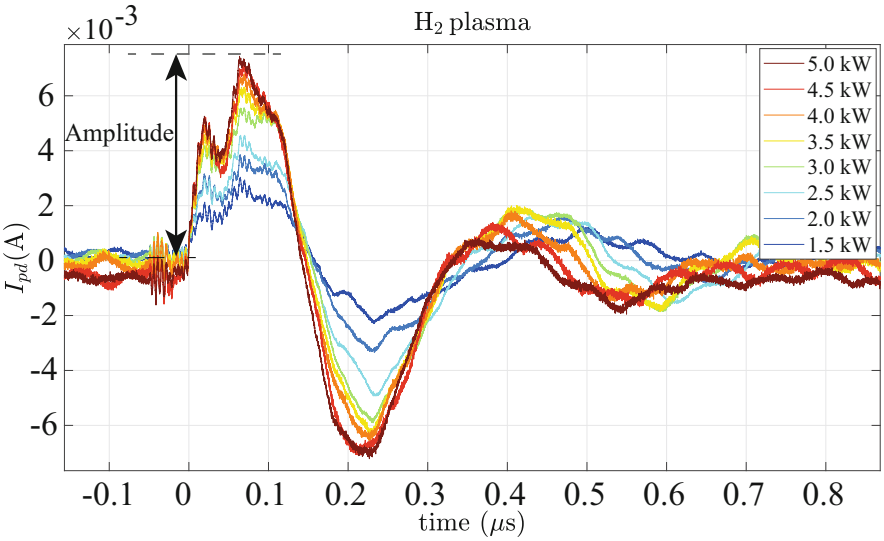

Fig. 9.9 Typical photodetachment signals for a H_2 plasma. The laser strikes the LP tip at $t = 0$ s causing the overshoot whose amplitude is indicated by the arrow. Reproduced from Agnello et al. (2020) with IAEA permission

and S. Aleiferis (2016). This effect is partly due to the motion of ions caused by the thermal motion of the electrons (Friedland et al. 1994). The large undershoot and the double peak might also be an effect of the different dynamics of the electrons, and the ions at the LP. Electrons are magnetized, having a Larmor radius which is comparable to, or smaller than, the LP radius of 0.2 mm. Ion trajectories, however, are not magnetically confined to the probe area because, in a magnetic field of 200 G, they have an ion Larmor radius of ∼1.6 mm, much bigger than the LP tip radius (Agnello et al. 2020). Numerical simulations using a particle-in-cell code have been performed to model the temporal dynamics of the observed photodetachment signal (Oudini et al. 2021). If the laser pulse strikes the probe when there is no plasma, no variation of the signal is detected. The amplitude increases with RF power confirming the trend observed during CRDS tests.

9.4 Measurements of Negative Ions

Experimental activities on RAID investigate the formation of negative ions by volumetric processes in H/D plasmas. By continuously improving the diagnostics, theory, and simulation tools, research on RAID has reached a level at which quantitative comparisons between theory and experiments can now be performed. Negative ions measured by OES, CRDS, and LPLP are reviewed here.

9.4.1 First Evidence of Negative Ions in RAID Using OES

An optical emission spectroscopy campaign performed in RAID in 2017 gave the first hints of the presence of negative hydrogen ions in RAID plasma (Marini et al. 2017). The first Balmer lines α, β, and γ and the Fulcher-α band were measured for both H_2 and D_2 plasmas. The radiance profiles were Abel inverted to obtain the absolute emissivity radial profiles. The absolute line emissivities were then interpreted with the collisional radiative code YACORA (Wünderlich et al. 2006) to estimate the degree of dissociation, the density profiles of atomic and molecular species and of the ions, including H^- and D^-. YACORA solves the rate equations for 40 states of H, taking into account the excitation and de-excitation by electron collision, the spontaneous emission, the recombination of H^+, the dissociation of H_2, and the mutual neutralization of H^- with the positive ions. Three-body reactions are also taken into account. However, the opacity is neglected because of the low pressure (0.3 Pa). Figure 9.10 shows in (a) the degree of dissociation, in (b) the degree of ionization, in (c) the density of H^+, and in (d) the density of H^-. The degrees of dissociation and ionization are defined, respectively, as

$$D_d = \frac{\frac{n_H}{n_{H_2}}}{\frac{n_H}{n_{H_2}} + 2}; \quad D_i = \frac{n_e}{n_H + n_{H_2}}. \tag{9.2}$$

As defined, D_i takes no account of the presence of negative ions in the plasma, and D_i would vary from zero, with no ionization, to infinity, when there are no neutral particles in the plasma. Therefore, this definition is only valid for low ionization rates with negligible negative ion densities. The dissociation is quite flat in the center of the plasma column around 20%, and the ionization is peaked at the center reaching about 0.7%. Also, n_{H^+} is narrow peaked at the center reaching $2 \times 10^{17}\,m^{-3}$. The most interesting plot is that of the density of the negative ions H^-, showing an off-axis peak at ~4 cm, where the density reaches $2 \times 10^{16}\,m^{-3}$. These measurements were the first evidence of volume produced negative ions in RAID and motivated the design of the laser-based diagnostics discussed in Sects. 9.3.2.2 and 9.3.2.4, namely CRDS and LPLP.

9.4.2 Measurements of Negative Ions Using CRDS

In this section, we describe the results obtained using CRDS published in Ref. Agnello et al. (2020). The purpose of the experiments was to perform parametric scans in RF power, magnetic field, and gas pressure, to investigate the behavior of the source at higher powers (up to 8 kW) as well as to optimize the CRDS technique. Figure 9.11 shows measurements of the negative ion density in H_2 and D_2 plasmas for different RF powers and gas pressures. CRDS data were analyzed employing the technique described in Sect. 9.3.2.3. H^- and D^-

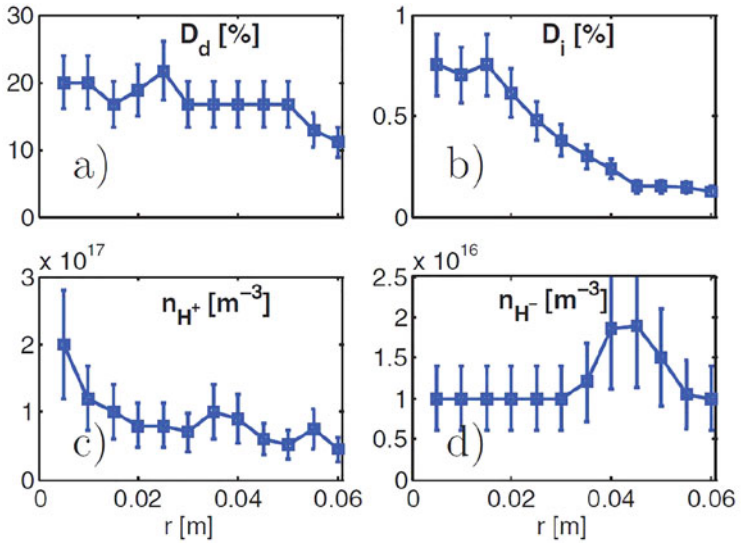

Fig. 9.10 (**a**) Degree of dissociation, (**b**) degree of ionization, (**c**) density of H^+, and (**d**) density of H^-, estimated by YACORA for an input power of 3 kW in hydrogen in RAID. Reproduced from Marini et al. (2017) with IAEA permission

line-integrated density increases with RF power for both plasmas. For power larger than 4 kW, however, the growth rate is reduced for H^-. Note that these values are obtained in cw operation on RAID, so the production of negative ions is in steady state. RAID operation at 0.2 Pa is possible, but this results in less negative ion production, and therefore the following experimental investigations were performed at 0.3 Pa.

9.4.3 Measurements of Negative Ions with LPLP

LPLP was also used to perform negative ion measurements in the plasmas of Sect. 9.4.2. Figure 9.12 summarizes the results obtained with laser photodetachment while varying the RF power. Measurements were performed for $0.04 < r < 0.065$ m because I_{dc} was too high and risked damaging the probe for small radii, and the window height limited the LOS of the laser at large radius. The left and the right columns show the results for H_2 and D_2 plasmas, respectively. In Fig. 9.12a, the amplitudes of the photodetachment signals are shown. On average, a weaker signal is measured in the case of D_2. Figure 9.12b shows the electron current I_{dc} when the probe is biased at $V_{\mathrm{bias}} = 26$ V above the plasma potential. On average, more electrons are collected in the case of D_2 suggesting that the electron density is higher in these plasmas. Figure 9.12c shows the ratios $n_{\mathrm{H^-}}/n_e$ and $n_{\mathrm{D^-}}/n_e$. Although the

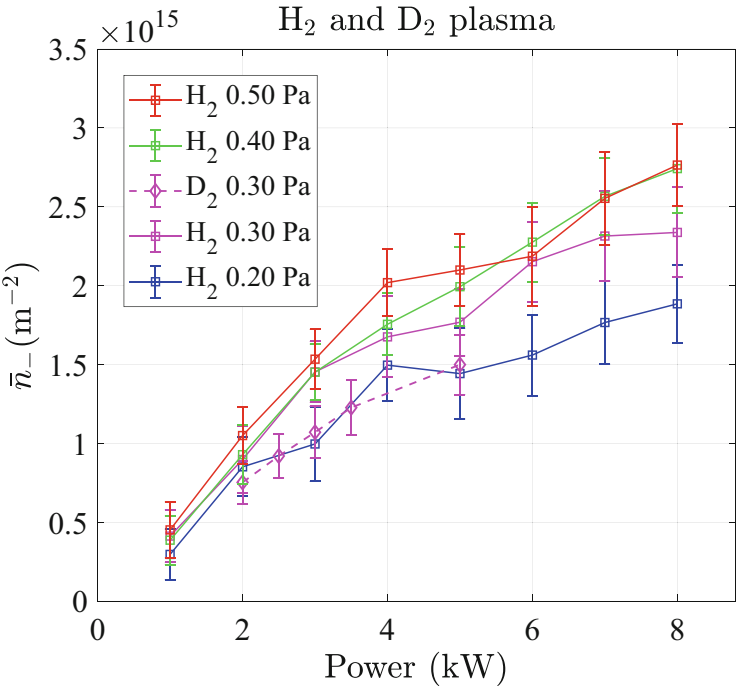

Fig. 9.11 Line-integrated negative ion density as a function of RF power at different pressures for H_2 and D_2 plasmas, demonstrating the steady-state production of negative ions up to 8 kW of RF power. Reproduced from Agnello et al. (2020) with IAEA permission

electrons are magnetized, the electron transport coefficient is the same both for the photodetached electrons and for the electrons collected by the probe when biased above V_{plasma}. This is justified as follows: the background electrons have an energy of about 1.5 eV in this region of the plasma column, and the photodetached electrons are released into the plasma with an energy of ∼0.45 eV. Thus, the ratio of the Larmor radii of the two types of electrons in the local magnetic field will be ∼1.7, and the transport of the electrons in that field should be similar. At $r = 0.06$ m, n_{H^-}/n_e reaches 0.3, while n_{D^-}/n_e reaches about 0.05. Also, the profile ratios are only weakly dependent on power, as shown in Fig. 9.12c. The independence of the ratio n_-/n_e from the RF power might be an advantage for negative ion extraction because it makes the negative ion yield in the source easier to tune. The difference between n_{H^-}/n_e and n_{D^-}/n_e arises mainly because the electron densities in D_2 plasmas are approximately a factor 3 higher than in H_2 plasmas for the same RF power, as shown in Fig. 9.12d, which means that the D^- and H^- densities are similar, for the same RF power, in the D_2 and H_2 plasmas in RAID. At 5 kW power and $r = 0.04$ m (where the fixed LOS of CRDS is located), n_e reaches $\sim 1.3 \times 10^{17}$ m^{-3} in H_2 and $\sim 2.9 \times 10^{17}$ m^{-3} in D_2. Although the absolute value of n_e might be unreliable because of electron magnetization, this data completes the

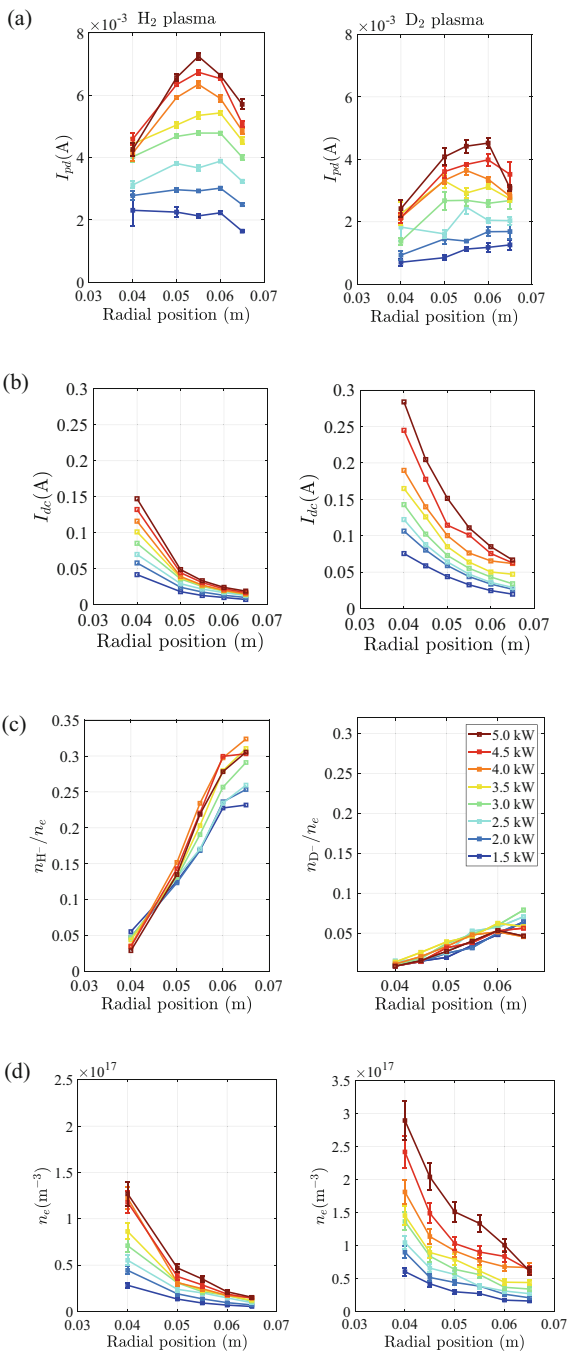

Fig. 9.12 Results of the laser photodetachment measurements for H_2 (left column) and D_2 (right column) plasmas at 0.3 Pa. (**a**) Photodetachment amplitudes I_{pd}, (**b**) electron current I_{dc} collected when the probe is biased at $V_{\text{bias}} = 26$ V above the plasma potential, (**c**) ratio n_-/n_e, and (**d**) electron density n_e. On the edge of the plasma column, hydrogen plasmas have lower electron density and a higher ratio n_-/n_e. Reproduced from Agnello et al. (2020) with IAEA permission

set of quantities that can be obtained only relying on the LP laser photodetachment technique. The higher density in D_2 is also measured by microwave interferometry at the edge, at the measurement position $r = 0.04$ m, revealing a line-integrated density a factor 2 higher in the case of deuterium.

The n_e profiles are obtained from the analysis of IV curves measured with the same LP used for laser photodetachment. The electron energy distribution function (EEDF) is calculated using the Druyvesteyn formula (Druyvesteyn 1930), and the second derivative of the measured electron current is calculated with a Savitzky–Golay filter to obtain the floating and plasma potential. An effective electron temperature T_e and the total electron density are then obtained by numerically integrating the EEDF. More details of the analysis can be found in Béchu et al. (2013). The data shown in Fig. 9.12a, b, and d can be used to calculate the negative ion density. The negative ion density peaks at $r \sim 0.055$ m and H^- and D^- are distributed in a shell-like shape, as also measured by OES. The peak density of H^- is $7.7 \times 10^{15}\,\mathrm{m}^{-3}$, which is a factor of ~2.5 lower compared to $2.0 \times 10^{16}\,\mathrm{m}^{-3}$ measured via OES (Marini et al. 2017). The disagreement between OES and laser photodetachment might be due to an incorrect estimate of n_e via LPs.

9.4.4 *Combining CRDS and LPLP to Extract Absolute Negative Ion Density Profiles*

In this section, we focus only on the data at 0.3 Pa since this is the pressure relevant to present NBI systems, such as the system designed for ITER, although lower pressure may be more relevant for future systems (Hemsworth et al. 2017). The measurement of n_e via LPs in a plasma with magnetized electrons might lead to error on the final estimate of negative ion density. To overcome this problem, we can use the line-integrated negative ion density measured using CRDS for absolute calibration. Using a form factor approach (Agnello et al. 2020), one can deduce n_-^{peak}, which provides the absolute negative ion density profile. The results are summarized by Fig. 9.13 showing n_{H^-} and n_{D^-} profiles. Only 2, 3, and 5 kW RF powers are shown for clarity. The peak value obtained at 5 kW for H_2 is $1.9\,(\pm 0.3) \times 10^{16}\,\mathrm{m}^{-3}$, close to the value measured by OES (Marini et al. 2017), which was $3.0\,(\pm 0.8) \times 10^{16}\,\mathrm{m}^{-3}$. For D^-, the peak value for 5 kW results in $1.8\,(\pm 0.3) \times 10^{16}\,\mathrm{m}^{-3}$, smaller than $4.5\,(\pm 2.0) \times 10^{16}\,\mathrm{m}^{-3}$ measured with OES. The discrepancy is probably due to errors in the deuterium cross-sections used in the OES analysis. More accurate deuterium cross-sections are now available in the recent analysis of Laporta et al. (2021). In Fig. 9.14, we plot the peak value of n_- for increasing powers, showing a linear trend, and the negative ion density with electron density measured by the LP at $r = 0.055$ m, close to n_- peak values. n_- increases almost linearly with n_e, and higher values may be attained by increasing the RF power. The lower ratio n_-/n_e in the case of deuterium is clearly visible. This suggests that the co-extracted electrons might be a more important issue for

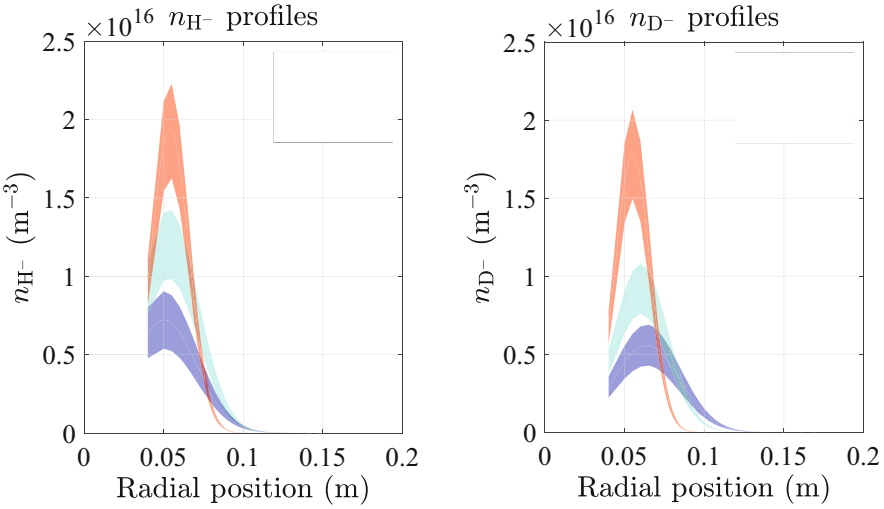

Fig. 9.13 n_{H^-} and n_{D^-} radial profiles for different powers obtained using the relative negative ion profiles measured with laser photodetachment and calibrated with CRDS line-integrated measurements. Reproduced from Agnello et al. (2020) with IAEA permission

D^- extraction. The isotopic effect in negative ion and electron density has been investigated by some authors (Skinner et al. 1993; Bruneteau et al. 1996; Fukumasa and Yoshino 1998), and it is due to a combination of different phenomena which we briefly explain as follows: calculations and experiments show that n_e is higher in deuterium than in hydrogen plasmas, which is mostly due to ion transport. Positive ions are indeed mostly lost by transport to the walls where they are neutralized. For deuterium, the transport of positive ions is a factor $1/\sqrt{2}$ smaller than for hydrogen because of the mass difference. This might explain in part the higher n_e in deuterium (Skinner et al. 1993). Concerning the isotope effect on the negative ion density, the lower value in deuterium might be due to the higher degree of dissociation in deuterium leading to increased cooling of $D_2(v)$ in collision with D and then less efficient D^- production (Skinner et al. 1993). For a better understanding of the processes, modeling is envisaged, which is the subject of the next section.

9.5 A 1.5D Fluid: Monte Carlo Model of a Hydrogen Helicon Plasma

To advance the understanding of the physics underlying the generation and transport of H^- and D^- in RAID, we use numerical simulations coupled to experimental data in this section. While a full description of the helicon wave propagation and power absorption coupled to a transport/chemistry model would be the ultimate

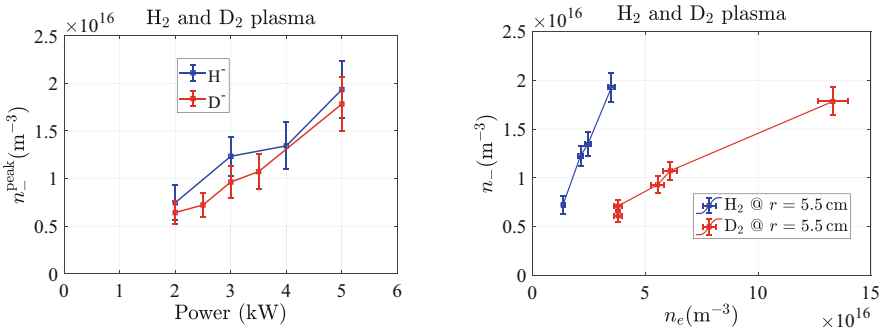

Fig. 9.14 Left: peak negative ion density as a function of RF power at 0.3 Pa. Right: negative ion density vs. electron density in hydrogen and deuterium plasmas. n_- increases with power, and higher density is observed in the case of H^-. Reproduced from Agnello et al. (2020) with IAEA permission

goal, this is clearly beyond the scope of the present work. Instead, we develop a model that combines two separately self-consistent approaches: a plasma fluid model calculating ion transport and a Monte Carlo (MC) model to determine neutral and ro-vibrational density profiles of H_2. Using the electron density and temperature profiles measured by Langmuir probes as input data, the densities of H^+, H_2^+, H_3^+, and H^- are computed in a 1.5D (dimensional) geometry.

The fluid approach can be applied in RAID since the ion-neutral collision mean free path (mfp) is smaller than the typical size of the device. The magnetic field can play an important role in plasma transport in low-pressure plasma sources (Hagelaar and Oudini 2011). Typical values of RAID magnetic field are such that the ion and electron Larmor radii are much smaller than the vessel radius of 20 cm (see Sect. 9.3.2.4), and therefore the plasma in RAID is strongly magnetized. It is assumed that the plasma species are diluted in a H_2 background. Ion transport is then described by classical drift–diffusion equations in the presence of a uniform magnetic field.

9.5.1 Description of the Fluid Model

Conservation of mass and momentum and Poisson's equations are used in the fluid description. Each ion species is denoted by the subscript s for H^+, H_2^+, H_3^+, or H^-. The equations are:

$$\nabla \cdot \mathbf{\Gamma_s} = S_s - L_s,$$
$$0 = q_s n_s (\mathbf{E} + \mathbf{u}_s \times \mathbf{B}) - k_b T_s \nabla n_s - m_s n_s \nu_s \mathbf{u_s},$$

$$\nabla^2 V = -\frac{e}{\epsilon_0}(n_{H^+} + n_{H_2^+} + n_{H_3^+} - n_{H^-} - n_e), \tag{9.3}$$

where n_s is the number density, m_s the mass, $\mathbf{u_s}$ the fluid velocity of the species, $\mathbf{E} = -\nabla V$ the electric field, $\mathbf{B}$ the magnetic field, q_s the electron charge magnitude, $\mathbf{\Gamma_s} = n_s \mathbf{u}_s$ the species flux, ν_s the momentum collisional transfer frequency, and S_s and L_s the source and the loss terms. The magnetic field $\mathbf{B}$ is the DC field generated by the coils (200 G) since the magnetic field of the helicon wave is only a few Gauss (Guittienne et al. 2021). A steady-state plasma is considered, and the electron inertia is neglected compared to the combined effect of $\mathbf{E}$ and $\mathbf{B}$. The ion distribution function is considered isotropic, and the ion temperature gradient is neglected in the pressure term. Plasma quasi-neutrality is guaranteed by the electric field generated by the charge separation. Equation (9.3) is then solved using COMSOL Multiphysics (COMSOL 2018).

In RAID, the vessel walls are far from the edge of the plasma column and electrically conducting, suggesting that boundary conditions are mainly dominated by the end plates, where plasma losses and recombination processes occur (Shinohara et al. 1998; Fubiani et al. 2021). A rigorous description of wall losses would require a self-consistent treatment of the plasma sheath (a few millimeters in front of the wall) where quasi-neutrality is lost and strong electric fields appear. Instead, the ion boundary losses are computed using the Bohm criterion, which, for positive ions, is $\Gamma_{wall} = -n_s\sqrt{qT_e/(m_s \mathrm{e})}$. Negative ions are confined to the plasma bulk in electropositive plasmas (Chabert and Braithwaite 2011) owing to the typical low ion temperature ($\sim$0.1 eV), which prevents them from escaping from the plasma potential well. H^- ions are therefore entirely produced and destroyed in the plasma volume. In RAID, it is therefore crucial to understand their production and destruction channels, discussed in Sect. 9.5.4, and how they can be controlled to optimize negative ion yield.

9.5.2 Reaction Rates

In this model, binary reactions between electrons, neutrals, and ion species are considered. Three-body reactions are neglected in this low pressure regime. The reaction rate $R_{12} = k(T_1, T_2)n_1 n_2$ $\mathrm{m^{-3}s^{-1}}$ is regulated by a rate coefficient $k(T_1, T_2)$ dependent on the reactant temperatures T_1 and T_2 shown in Table 9.3. The channels for the volume production of H^- are given by reactions 3, 7, and 22, but dissociative attachment, 3, is by far the most effective channel for H^- production in the RAID plasma. The net source term for each ion species is reported in the following equations (Agnello et al. 2022):

Table 9.3 Plasma reactions and rates used for this fluid transport model. Reaction 3 is for vibrational states $v = 0 - 14$. For Reaction 3, the dissociative attachment reaction rate provided in Ref. Janev et al. (2003) was used; for the others, the reaction rates are provided in Ref. Santoso (2018). We note that for deuterium, the vibrational excitation and dissociation by electron impact were recently given in Laporta et al. (2021). From Agnello et al. (2022), copyright IOP Publishing. Reproduced with permission. All rights reserved

	Reaction	Reaction rate (k_n) [$m^3 s^{-1}$]
1	$e + H_2 \rightarrow H_2^+ + 2e$	$7.27 \cdot 10^{-15} T_e^{0.549} e^{-15.5/(T_e - 0.001)} + 1.37 \cdot 10^{-14} T_e^{-0.557} e^{-20.3/T_e}$
2	$e + H_2 \rightarrow 2H + e$	$1.54 \cdot 10^{-14} T_e^{0.06} e^{8.63/T_e} + 1.11 \cdot 10^{-13} T_e^{-0.813} e^{-13.4/T_e}$
3	$e + H_2 \rightarrow H + H^-$	$1.972 \sigma_v^{(0)} \frac{T_e^{1/2}}{1+T_e/E_0} e^{-\frac{\Delta E_{th,v}}{T_e}} \left[\frac{\lvert E_{th,v}\rvert}{T_e} + \frac{1}{1+T_e/E_0}\right] \times (10^{-14}))$
4	$e + H \rightarrow H^+ + 2e$	$9.74 \cdot 10^{-15} T_e^{-0.174} e^{-14.3/(T_e - 0.001)} + 6.35 \cdot 10^{-15} T_e^{0.433} e^{-16.4/T_e}$
5	$H + H_2^+ \rightarrow H_2 + H^+$	$1.54 \cdot 10^{-14} T_e^{-0.859} e^{-4.61/(T_1 - 0.786)} + 1.64 \cdot 10^{-15} T_i^{-0.353} e^{-0.258/T_i}$
6	$e + H_2^+ \rightarrow H + H^+ + e$	$3.50 \cdot 10^{-13} T_e^{-1.25} e^{-3.19/(T_e - 0.008)} + 1.77 \cdot 10^{-13} T_e^{-0.0924} e^{-3.04/T_e}$
7	$e + H_3^+ \rightarrow H_2^+ + H^-$	$1.93 \cdot 10^{-15} T_e^{-1.07} e^{-6.26/(T_e + 0.131)} + 5.35 \cdot 10^{-17} T_e^{-0.371} e^{-2.07/T_e}$
8	$H_2 + H_2^+ \rightarrow H + H_3^+$	$6.29 \cdot 10^{-15} T_i^{-1.46} e^{-2.22/(T_i + 0.356)} + 2.71 \cdot 10^{-16} T_e^{-1.30} e^{-0.317/T_i}$
9	$H^+ + H^- \rightarrow 2H$	$4.46 \cdot 10^{-14} T_i^{-0.281} + 1.26 \cdot 10^{-14} e^{-1.96/T_i}$
10	$H_2^+ + H^- \rightarrow H_2 + H$	$2.23 \cdot 10^{-14} T_i^{0.425} + 8.93 \cdot 10^{-14} T_i^{-0.261}$
11	$H_3^+ + H^- \rightarrow \frac{H_2}{2} + 3H$	$1.70 \cdot 10^{-14} T_i^{0.313} + 5.75 \cdot 10^{-14} T_i^{-0.288}$
12	$e + H^- \rightarrow H + 2e$	$4.58 \cdot 10^{-13} T_e^{0.287} e^{-4.41/(T_e + 0.117)} + 2.71 \cdot 10^{-14} T_e^{0.62} e^{-1.82/T_e}$
13	$e + H_3^+ \rightarrow 2H + H^+ + e$	$2.69 \cdot 10^{-13} T_e^{-0.245} e^{-15.6/(T_e + 0.003)} + 1.01 \cdot 10^{-12} T_e^{-0.464} e^{-26.8/T_e}$
14	$H_2 + H^+ \rightarrow H_3^+ + h\nu$	$1.63 \cdot 10^{21}$
15	$e + H_2^+ \rightarrow 2H$	$2.29 \cdot 10^{-14} T_e^{-0.571} + 3.31 \cdot 10^{-15} T_e^{-0.152 T_e}$
16	$e + H_3^+ \rightarrow 3H$	$3.36 \cdot 10^{-15} T_e^{-0.716} + 3.73 \cdot 10^{-14} T_e^{-0.67} e^{6.40/T_e}$
17	$e + H_3^+ \rightarrow H + H_2$	$2.03 \cdot 10^{-15} (T_e^{-0.189} + 0.04 T_e^{-1.49}) + 5.57 \cdot 10^{-14} T_e^{1.23} e^{-6.21/T_e}$
18	$H + H^- \rightarrow H_2 + e$	$2.16 \cdot 10^{-13} T_i^{-1.89} e^{-12.7/(T_i + 1.17)} + 1.30 \cdot 10^{-15} T_i^{-0.418} e^{-0.192/T_i}$
19	$H_2 + H^- \rightarrow H + H_2 + e$	$1.62 \cdot 10^{-16} T_i^{0.417} e^{-6.47/(T_i + 0.132)} + 5.70 \cdot 10^{-16} T_i^{0.550} e^{-2.19/T_i}$
20	$H + H^- \rightarrow 2H + e$	$3.81 \cdot 10^{-15} T_i^{0.280} e^{-3.76/(T_i + 0.626)} + 4.55 \cdot 10^{-16} T_i^{0.603} e^{-0.375/T_i}$
21	$H_2 + H^+ \rightarrow H + H_2^+$	$5.54 \cdot 10^{-16} T_i^{-0.453} e^{-3.26/(T_i - 0.001)} + 5.98 \cdot 10^{-18} T_i^{-2.88} e^{-0.310/T_i}$
22	$e + H \rightarrow H^- + h\nu$	$5.75 \cdot 10^{-20} (T_e^{-0.0285} - 0.94 T_e^{-0.05}) + 6.54 \cdot 10^{-19} T_e^{-5.18} e^{-72.4/T_e}$

$$\nabla \cdot \Gamma_{H^+} = k_4 n_e n_H + k_5 n_H n_{H^+} + k_6 n_e n_{H_2^+} - k_9 n_{H^+} n_{H^-} + k_{13} n_e n_{H_3^+} - k_{14} n_{H_2} n_H - k_{21} n_{H_2} n_{H^+},$$

$$\nabla \cdot \Gamma_{H_2^+} = k_{11} n_e n_{H_2} - k_5 n_H n_{H_2^+} - k_6 n_e n_{H_2^+} + k_7 n_e n_{H_3^+} - k_8 n_{H_2} n_{H_2^+} - k_{10} n_{H_2^+} n_{H^-} - k_{15} n_e n_{H_2^+} + k_{21} n_{H_2} n_{H^+},$$

$$\nabla \cdot \Gamma_{H_3^+} = -k_7 n_e n_{H_3^+} + k_8 n_{H_2} n_{H_2^+} - k_{11} n_{H_3^+} n_{H^-} - k_{13} n_e n_{H_3^+} + k_{14} n_{H_2} n_{H^+} - k_{16} n_e n_{H_3^+} - k_{17} n_e n_{H_3^+},$$

$$\nabla \cdot \Gamma_{H^-} = n_e \sum_{\nu=0}^{14} k_3(\nu) n_{H_2(\nu)} + k_7 n_e n_{H_3^+} - k_9 n_{H^+} n_{H^-} - k_{10} n_{H_2^+} n_{H^-} - k_{11} n_{H_3^+} n_{H^-} - k_{12} n_e n_{H^-} - k_{18} n_H n_{H^-} - k_{19} n_{H_2} n_{H^-} - k_{20} n_H n_{H^-} + k_{22} n_e n_H.$$

The term $\sum_{\nu=0}^{14} k_3(\nu) n_{H_2(\nu)}$ describes the generation rate of H^- by dissociative attachment from ro-vibrationally excited H_2 and is calculated by taking into account the density of H_2 molecules in each vibrational state ν, computed by the MC model (see Sect. 9.5.3). The most important H^- destruction processes are the mutual neutralization (MN) with positive ions (R9–11), the electron detachment (ED) (R12), and the associative detachment (AD) with neutrals (R18–20). Measured electron temperature and density from LPs and microwave interferometry are used as input to compute transport and chemistry. Figure 9.15 shows typical profiles 1 m from the antenna, for 3 kW RF power and 0.3 Pa.

Molecular hydrogen can be ro-vibrationally excited by electron impact or by decay from the excited molecule, sustaining 15 vibrational states in the electronic ground state. Experimental and theoretical studies have revealed that dissociative attachment to these vibrationally excited states is the main mechanism responsible for volume production of negative ions (Bacal 2006; Bacal et al. 2021). A full description of the hydrogen plasma would include collisions between H_2 in its various ro-vibrational states and other plasma species. This would complicate the model without significantly changing the ion transport. Since for RAID plasma, only about 1% of H_2 is excited compared to background H_2 (Fubiani et al. 2017), the overall ion transport and chemistry will be only weakly influenced by the excited H_2. To approximate the contribution of the dissociative attachment to H^- production, the MAR (molecular activated recombination) rate coefficient could be used as a reasonable approximation for the dissociative attachment reaction rate (Pigarov and Krasheninnikov 1996). In this study, however, we use a Monte Carlo model to estimate the radial density profiles of each ro-vibrational state of H_2 which are then inserted as input into the fluid model.

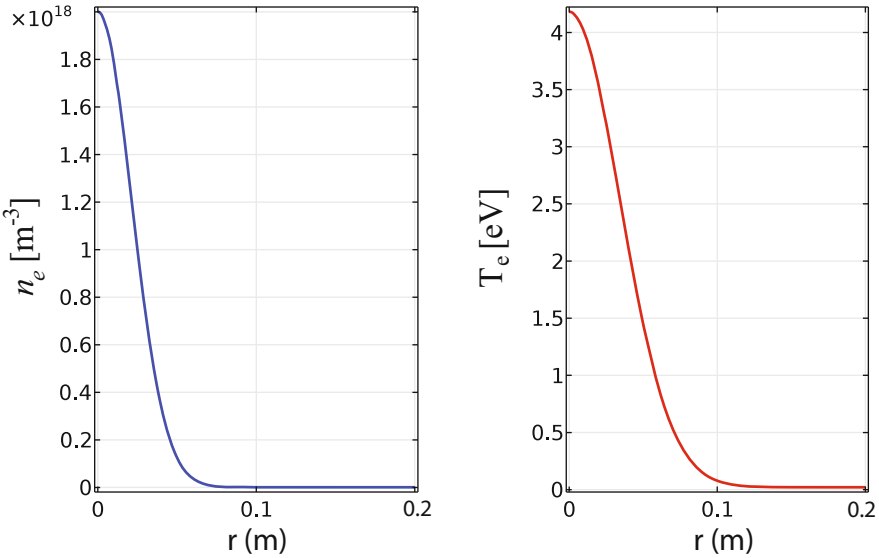

Fig. 9.15 Electron density and temperature radial profiles used as input in the model, obtained by fitting experimental data (Agnello 2020). These profiles are representative for a hydrogen plasma discharge with 3 kW RF power and 0.3 Pa gas pressure at 1 m from the center of the antenna. From Agnello et al. (2022), copyright IOP Publishing. Reproduced with permission. All rights reserved

9.5.3 A Monte Carlo (MC) Model to Determine Neutral Density Profiles

To improve the self-consistency of the model, the plasma dynamics is coupled with the H_2 vibrational kinetics because the H^- production depends strongly on the molecular vibrational distribution function (VDF). A Monte Carlo (MC) approach is used considering the charged particles as a fixed background with non-uniform density and temperature distributions obtained from the plasma fluid model. This gas–plasma decoupling is a necessary hypothesis due to the very different plasma and gas kinetic time scales, μs and ms, respectively.

The MC model (Taccogna et al. 2007) is 1D in the radial direction keeping the same geometrical reduction arguments used for the plasma fluid model. The simulation starts with a uniform radial distribution of molecules; at each time step, a certain number of molecules are injected uniformly along the radial domain to keep the number of molecules fixed. This mimics the continuous axial flow of molecules keeping the gas pressure constant. Each particle contains information about its electronic (for atoms) and ro-vibrational (for molecules) state. Only the fundamental electronic state of H_2 is taken into account. Rotational states are not considered since the high ionization coefficient and the electron temperature guarantee a rotational equilibrium. The most relevant collisions with electrons and H^+ ions (the dominant ion species, see Sect. 9.5.4) are considered through the use

of state selective cross-sections (Celiberto et al. 2001; Krstic and Schultz 2003; Hunter and Kuriyant 1977), while neutral–neutral collisions are negligible due to the low pressure regime. The equations of motion of particles are solved, and surface processes are modeled by using appropriate coefficients (Kim et al. 1999; Rutigliano et al. 2014). For molecules, relaxation and dissociation coefficients are taken from Billing and Cacciatore (1995); Hiskes and Karo (1989). The gas subsystem reaches a steady-state condition after 4 ms. The radial averaged VDF shows the typical parabolic Treanor behavior for the first 4 vibrational levels and hyperbolic plateau for $\geq$ 4, corresponding to a two-temperature distribution $T_{01} = 2000\,\mathrm{K}$ and $T_{07} = 7000\,\mathrm{K}$. Once the n_H and n_{H_2} radial density profiles have been determined, the degrees of ionization and dissociation (9.2) can be computed; the degree of ionization is peaked at the center where it reaches about 2%. This is qualitatively similar to the OES result in Fig. 9.10b, although about 3 times larger. Given the very different methods, experimental errors, and rate constant uncertainties, this discrepancy is not unexpected. The degree of dissociation is slightly hollow at the center and $\approx 10\%$ across the vessel, and thus the H_2 molecular density is dominant, satisfying the fluid model assumption of plasma species diluted in a H_2 background.

9.5.4 Transport of the Ion Species

Solution of the coupled equations Eq. (9.3) yields the density of each ion species, Fig. 9.16, together with the net source rate profiles (production–destruction) for H^+, H_2^+, H_3^+, and H^-. H^+ and H_2^+ show centrally peaked density profiles, while H_3^+ peaks at the column edge at $r \approx 5\,\mathrm{cm}$. The H^- density profile also shows a shell-like structure, whose density and ≈ 1 cm width are comparable to measurements by laser-based diagnostics (Agnello et al. 2020). At the position of the H^- density peak, H_2^+ and H_3^+ densities are also comparable to that of H^+. This shows that the plasma column is characterized by a hot and dense core of ionizing plasma dominated by H^+ and H_2^+, surrounded by a ring of H_3^+ and H^-. The peak density is sensitive to axial losses which are not self-consistently calculated here. To have an insight on plasma species radial transport, Fig. 9.17 shows the absolute values and direction of the radial flux for each plasma species. H^+ and H_2^+ fluxes peak at about 2 cm from the center and are lost in a few centimeters due to volume destruction processes with background gas. The net generation rate of H_3^+ occurs at a ring of radius 1 cm in Fig. 9.16a, and the outward drift in the radial electric field shown in Fig. 9.17 combines to give a ring profile of maximum H_3^+ density at 4.5 cm, as shown in Fig. 9.16b. H^- are transported inward across the radius.

In conventional negative ion sources for fusion, negative ion production is achieved in two steps in separate volumes: a *driver* region where molecular hydrogen (or deuterium) is dissociated and an *expansion* region with a cesiated surface where H/D atoms attach electrons. In the case of a Cs-free negative ion source such as RAID, where negative ions are produced only in the plasma volume, it is interesting to study the contribution of production and destruction processes

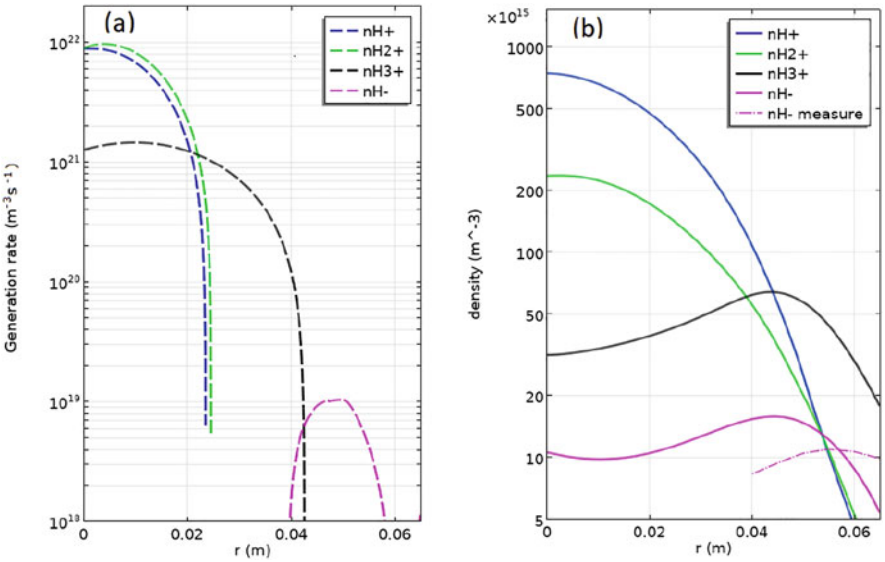

Fig. 9.16 (**a**) Net generation rate and (**b**) density profiles of ion species computed by the fluid model, including experimental n_{H^-} data. From Agnello et al. (2022), copyright IOP Publishing. Reproduced with permission. All rights reserved

along the radial direction. Figure 9.18 shows the reaction rates for H^- production (dashed lines) and destruction processes (solid lines) for electron collision reactions on the left and for reactions involving only heavy species on the right. The dissociative attachment reaction from H_2 ro-vibrational excited states is the main contributor to negative ion production (Bacal et al. 2021). The main destruction processes in the plasma center are electron detachment and mutual neutralization with H^+. However, at the edge of the plasma column, where H^- peaks ($r \approx 5$ cm), the most important destruction channels are associative detachment and mutual neutralization with H_3^+ and H_2^+. Thus, negative ions are mostly produced on axis but are efficiently destroyed by electron detachment. They mostly survive on the edge of the column because T_e is lower so that a net creation of H^- occurs as shown in Fig. 9.16, which gives the sum of all the production and destruction rates for H^-.

9.6 Conclusions

The present work broadens the knowledge of the plasma in a high-power helicon plasma source and provides new insights into the generation and transport of negative ions in linear helicon devices supported by numerical simulations. By developing dedicated state-of-the-art diagnostics on RAID, we can now perform detailed measurements of electron temperature and density profiles together with

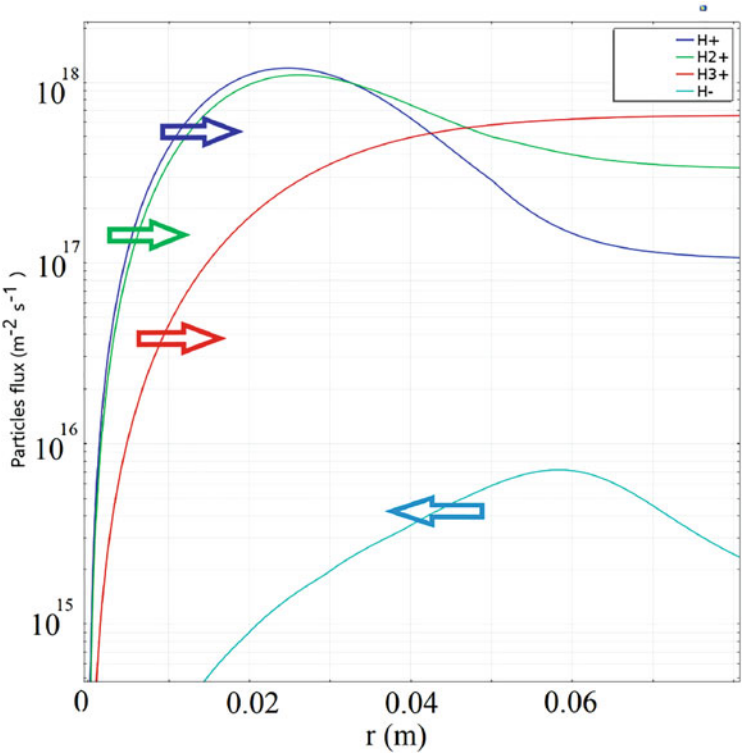

Fig. 9.17 Fluxes of ions across the radius are dominated by drift in the outward radial electric field. Positive ions are therefore transported outwards, whereas H^- are transported inward and destroyed by electron detachment and mutual neutralization with positive ions. From Agnello et al. (2022), copyright IOP Publishing. Reproduced with permission. All rights reserved

absolute measurements of negative ion density profiles in hydrogen and deuterium helicon plasmas. These experimental results are compared with numerical simulations using a 1.5D fluid model describing ion transport and chemistry of the hydrogenic species. We discovered that in RAID negative ions have a net production rate in a shell at the edge of the plasma column from where they diffuse toward the axis. H^- are mainly destroyed in the plasma center by electron detachment and are mainly neutralized by associative detachment at the edge. Future developments on H^- volume production in helicon sources should investigate the optimal balance between the various competing mechanisms to maximize the volume density of H^- close to the extraction region. In parallel, we will continue improving the set of diagnostics, in particular with the development of a two-photon laser-induced fluorescence (TALIF) system, which will allow precise experimental measurements of atomic hydrogen and deuterium to reach a better understanding of the physics of volumetric H-/D- production in helicon plasmas.

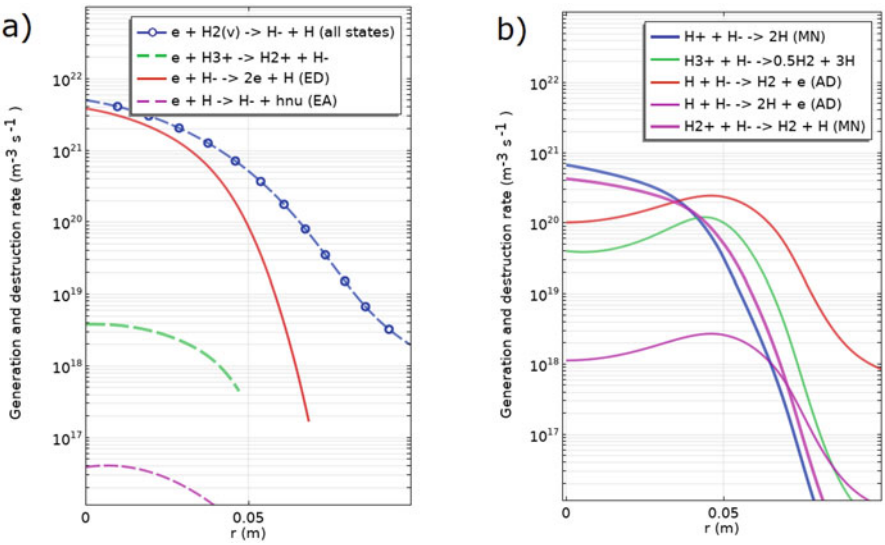

Fig. 9.18 Individual production (dotted lines) and destruction (continuous lines) processes of H^- along the radius (**a**) caused by electrons and (**b**) caused by ions and neutrals. The dissociative attachment from ro-vibrationally excited H_2 is the dominant production process. In the plasma center, H^- is mainly detached by electron impact, while at the edge, mutual neutralization processes with positive ions and associative detachment are the main loss reactions. From Agnello et al. (2022), copyright IOP Publishing. Reproduced with permission. All rights reserved

Acknowledgments This work has been carried out within the framework of the EUROfusion Consortium and has received funding from the Euratom research and training program 2014–2018 and 2019–2020 under grant agreement No 633053. The views and opinions expressed herein do not necessarily reflect those of the European Commission. This work was supported in part by the Swiss National Science Foundation.

References

R. Agnello, *Negative Hydrogen Ions In a Helicon Plasma Source*. PhD thesis (EPFL, Switzerland, 2020)

R. Agnello, Y. Andrebe, H. Arnichand, P. Blanchard, T.D. Kerchove, I. Furno, A.A. Howling, R. Jacquier, A. Sublet, Application of Thomson scattering to helicon plasma sources. J. Plasma Phys. **86**, 905860306 (2020)

R. Agnello, M. Barbisan, I. Furno, P. Guittienne, A.A. Howling, R. Jacquier, R. Pasqualotto, G. Plyushchev, Y. Andrebe, S. Béchu, I. Morgal, A. Simonin, Cavity ring-down spectroscopy to measure negative ion density in a helicon plasma source for fusion neutral beams. Rev. Sci. Instrum. **89**, 103504 (2018)

R. Agnello, S. Béchu, I. Furno, P. Guittienne, A.A. Howling, R. Jacquier, G. Plyushchev, M. Barbisan, R. Pasqualotto, I. Morgal, A. Simonin, Negative ion characterization in a helicon plasma source for fusion neutral beams by cavity ring-down spectroscopy and Langmuir probe laser photodetachment. Nucl. Fusion **60**, 026007 (2020)

R. Agnello, G. Fubiani, I. Furno, P. Guittienne, A. Howling, R. Jacquier, F. Taccogna, A 1.5D fluid—Monte Carlo model of a hydrogen helicon plasma Plasma Phys. Control. Fusion **64**, 055012 (2022)

S. Aleiferis, *Experimental Study of* H^- *Negative ion Productionby Electron Cyclotron Resonance Plasmas*, PhD thesis (Université Grenoble-Aples, Grenoble, 2016)

M. Bacal, Photodetachment diagnostic techniques for measuring negative ion densities and temperatures in plasmas. Rev. Sci. Instrum. **71**, 3981 (2001)

M. Bacal, Physics aspects of negative ion sources. Nucl. Fusion **46**, S250–S259 (2006)

M. Bacal, M. Sasao, M. Wada, Negative ion sources. J. Appl. Phys. **129**, 221101 (2021)

F.E. Baghiti-Sube, F. Basht, M. Bacal, Photodetachment diagnostics of plasma with a high n_-/n_e ratio. Rev. Sci. Instrum. **67**, 2221 (1996)

S. Béchu, A. Soum-Glaude, A. Bès, A. Lacoste, P. Svarnas, S. Aleiferis, A.A. Ivanov, M. Bacal, Multi-dipolar microwave plasmas and their application to negative ion production. Phys. Plasmas **20**, 101601 (2013)

M. Berger, U. Fantz, S. Christ-Koch, NNBI Team, Cavity ring-down spectroscopy on a high power RF driven source for negative hydrogen ions. Plasma Sources Sci. Technol. **18**(2), 025004 (2009)

G.D. Billing, M. Cacciatore, Recombination coefficient and final state vibrational distribution for the reaction: H+Had+Cu(111)=H2(v)+Cu(111), in *7th International Symposium on Production and Neutralization of Negative Ions and Beams, AIP Conference Proceedings*, vol. 380(118) (1995)

R.W. Boswell, Plasma production using a standing helicon wave. Phys. Lett. **33A**(7), 457–458 (1970)

A.M. Bruneteau, C. Courteille, R. Leroy, M. Bacal, Investigation of two negative hydrogen and deuterium ion sources: Effect of the volume. Rev. Sci. Intrum. **67**, 3827 (1996)

R. Celiberto, R.K. Janev, A. Laricchiuta, M. Capitelli, J.M. Wadehra, D.E. Atems, Cross section data for electron-impact in elastic processes of vibrationally excited molecules of hydrogen and its isotopes. At. Data Nucl. Data Tables **77**, 161 (2001)

P. Chabert, N. Braithwaite, *Physics of Radio-Frequency Plasmas* (Cambridge University Press, Cambridge, 2011)

S. Christ-Koch, U. Fantz, M. Berger, NNBI Team, Laser photodetachment on a high power, low pressure rf-driven negative hydrogen ion source. Plasma Sources Sci. Technol. **18**(2), 025003 (2009)

COMSOL, Multiphysics® v. 5.6. (2018)

P. Devynck, J. Auvray, M. Bacal, P. Berlemont, J. Bruneteau, R. Leroy, R.A. Stern, photodetachment technique for measuring H- velocities in a hydrogen plasma. Rev. Sci. Intrum. **50**, 2944 (1989)

M.J. Druyvesteyn, Der Niedervoltbogen. ZS. f. Phys. **69**, 781 (1930)

U. Fantz, H. Falter, P. Franzen, D. Wünderlich, M. Berger, A. Lorenz, W. Kraus, P. McNeely, R. Riedl, E. Speth, Spectroscopy—a powerful diagnostic tool in source development. Nucl. Fusion **46**(6), S297–S306 (2006)

L. Friedland, C.I. Ciubotariu, M. Bacal, Dynamic plasma response in laser-photodetachment experiments in hydrogen plasmas. Phys. Rev. E **49**, 4353 (1994)

G. Fubiani, R. Agnello, I. Furno, L. Garrigues, P. Guittienne, G. Hagelaar, A. Howling, R. Jacquier, B. Reman, A. Simonin, F. Taccogna, Negative hydrogen ion dynamics inside the plasma volume of a linear device: Estimates from particle-in-cell calculations. Phys. Plasmas **28**, 063503 (2021)

G. Fubiani, L. Garrigues, G. Hagelaar, N. Kohen, J.P. Boeuf, Modeling of plasma transport and negative ion extraction in a magnetized radio-frequency plasma source. New J. Phys. **19**(1), 015002 (2017)

O. Fukumasa, K. Yoshino, Isotope effect and cesium dependence of negative ion production in volume and ion sources. Rev. Sci. Intrum. **69**, 941 (1998)

I. Furno, R. Agnello, U. Fantz, A. Howling, R. Jacquier, C. Marini, G. Plyushchev, P. Guittienne, A. Simonin, Helicon wave-generated plasmas for negative ion beams for fusion. EPJ Web of Conferences **157**, 03014 (2017)

P. Guittienne, E. Chevalier, C. Hollenstein, Towards an optimal antenna for helicon wave excitation. J. Appl. Phys. **98**, 083304 (2005)

P. Guittienne, R. Jacquier, B.P. Duteil, A.A. Howling, R. Agnello, I. Furno, Helicon wave plasma generated by a resonant birdcage antenna: magnetic field measurements and analysis in the RAID linear device. Plasma Sources Sci. Technol. **30**, 075023 (2021)

G.J.M. Hagelaar, N. Oudini, Plasma transport across magnetic field lines in low-temperature plasma sources. Plasma Phys. Control. Fusion **53**, 124032 (2011)

R.S. Hemsworth, D. Boilson, P. Blatchford, M.D. Palma, G. Chitarin, H.P.L. de Esch, F. Geli, M. Dremel, J. Graceffa, D. Marcuzzi, G. Serianni, D. Shah, M. Singh, M. Urbani, P. Zaccaria, Overview of the design of the ITER heating neutral beam injectors. New J. Phys. **19**(2), 025005 (2017)

J.R. Hiskes, A.M. Karo, Analysis of the h_2 vibrational distribution in a hydrogen discharge. Appl. Phys. Lett. **54**, 508 (1989)

A.T. Hjartarson, E.G. Thorsteinsson, J.T. Gudmundsson, Low pressure hydrogen discharges diluted with argon explored using a global model. Plasma Sources Sci. Technol. **19**(6), 065008 (2010)

M.B. Hopkins, K.N. Mellon, Enhanced production of negative ions in low-pressure hydrogen and deuterium discharges. Phys. Rev. Lett. **67**, 449 (1991)

G. Hunter, M. Kuriyant, Proton collisions with hydrogen atoms at low energies: Quantum theory and integrated cross-sections proton collisions with hydrogen atoms at low energies: Quantum theory and integrated cross-sections, in *Proceedings of the Royal Society of London. Series A, Mathematical and Physical Sciences*, vol. 353 (1977), pp. 575–588

R. Jacquier, R. Agnello, B.P. Duteil, P. Guittienne, A. Howling, G. Plyushchev, C. Marini, A. Simonin, I. Morgal, S. Bechu, I. Furno, First B-dot measurements in the RAID device, an alternative negative ion source for DEMO neutral beams. Fusion Eng. Des. **146**, 1140–1144 (2019)

R.K. Janev, D. Reiter, U. Samm, Collision Processes in Low-Temperature Hydrogen Plasmas. FZ-Jülich Report No. 4105 (2003)

Y. Kim, J. Ree, H. Shin, Formation of vibrationally excited hydrogen molecules on a graphite surface. Chem. Phys. Lett. **314**, 1 (1999)

P.S. Krstic, D.R. Schultz, Elastic processes involving vibrationally excited molecules in cold hydrogen plasmas. J. Phys. B: At. Mol. Opt. Phys. **36**, 385 (2003)

V. Laporta, R. Agnello, G. Fubiani, I. Furno, C. Hill, D. Reiter, F. Taccogna, Vibrational excitation and dissociation of deuterium molecule by electron impact. Plasma Phys. Control. Fusion **63**, 085006 (2021)

C. Marini, R. Agnello, B.P. Duval, I. Furno, A.A. Howling, R. Jacquier, A.N. Karpushov, G. Plyushchev, K. Verhaegh, P. Guittienne, Spectroscopic characterization of H_2 and D_2 helicon plasmas generated by a resonant antenna for neutral beam applications in fusion. Nucl. Fusion **57**, 036024 (2017)

S.H. Müller, A. Diallo, A. Fasoli, I. Furno, B. Labit, M. Podestà, Plasma blobs in a basic toroidal experiment: Origin, dynamics, and induced transport. Phys. Plasmas **14**, 110704 (2007)

H. Nakano, K. Tsumori, M. Shibuya, S. Geng, M. Kisaki, K. Ikeda, K. Nagaoka, M. Osakabe, Y. Takeiri, O. Kaneko, Cavity ringdown technique for negative-hydrogen-ion measurement in ion source for neutral beam injector. J. Instrum. **11**(03), C03018–C03018 (2016)

A. O'Keefe, D.G. Deacon, Cavity ring-down optical spectrometer for absorption measurements using pulsed laser sources. Rev. Sci. Intrum. **59**, 2544 (1988)

N. Oudini, A. Bendib, R. Agnello, I. Furno, F. Taccogna, Laser photo-detachment combined with Langmuir probe in magnetized electronegative plasma: how the probe size affects the plasma dynamic? Plasma Sources Sci. Technol. **30**, 115005 (2021)

A. Pigarov, S. Krasheninnikov, Application of the collisional-radiative, atomic-molecular model to the recombining divertor plasma. Phys. Lett. A **222**, 251–257 (1996)

T.K. Popov, M. Mitov, A. Bankova, P. Ivanova, M. Dimitrova, S. Rupnik, J. Kovačič, T. Gyergyek, M. Cerček, F.M. Dias, Langmuir probe method for precise evaluation of negative-ion density in electronegative gas discharge magnetized plasma. Contrib. Plasma Phys. **53**, 51–56 (2013)

M. Rutigliano, P. Gamallo, R. Sayos, S. Orlandini, M. Cacciatore, A molecular dynamics simulation of hydrogen atoms collisions on an H-preadsorbed silica surface. Plasma Sources Sci. Technol. **23**, 045016 (2014)

J.S. Santoso, *Production of Negative Hydrogen Ions in a High-Powered Helicon Plasma Source*. PhD thesis (Australian National University, Canberra, 2018)

S. Shinohara, N. Kaneda, Y. Kawai, Effects of antenna wavenumber spectrum and metal end plate on plasma characteristics excited by helicon wave. Thin Solid Films **316**, 139–147 (1998)

D.A. Skinner, A.M. Bruneteau, P. Berlemont, C. Courteille, R. Leroy, M. Bacal, Isotope effect and electron-temperature dependence in volume h and d ion sources. Phys. Rev. E **48**, 2122 (1993)

F. Taccogna, R. Schneider, S. Longo, M. Capitelli, Modeling of a negative ion source. I. Gas kinetics and dynamics in the expansion region. Phys. Plasmas **14**, 073503 (2007)

K. Takahashi, S. Takayama, A. Komuro, A. Ando, Standing helicon wave induced by a rapidly bent magnetic field in plasmas. Phys. Rev. Lett. **116**, 135001 (2016)

D. Thompson, R. Agnello, I. Furno, A. Howling, R. Jacquier, G. Plyushchev, E. Scime, Ion heating and flows in a high power helicon source. Phys. Plasmas **24**, 063517 (2017)

D. Wünderlich, D. Dietrich, U. Fantz, Application of a collisional radiative mode to atomic hydrogen for diagnostic purposes. J. Quant. Spectrosc. Radiat. Transf. **110**(1), 62–71 (2006)